Nano Research
2019, 12(4): 889–896

ISSN 1998-0124 CN 11-5974/O4
https://doi.org/10.1007/s12274-019-2319-6

Research Article

Regulation of the cellular uptake of nanoparticles by the orientation of helical polypeptides

Chong Zhang[1,2,§], Jianhua Lu[1,2,§], Falin Tian[3,§], Lindong Li[1,4], Yingqin Hou[1,2], Yaoyi Wang[1,2], Lingdong Sun[1,4] (✉), Xinghua Shi[3] (✉), and Hua Lu[1,2] (✉)

[1] *Beijing National Laboratory for Molecular Sciences, College of Chemistry and Molecular Engineering, Peking University, Beijing 100871, China*
[2] *Center for Soft Matter Science and Engineering, Key Laboratory of Polymer Chemistry and Physics of Ministry of Education, Peking University, Beijing 100871, China*
[3] *CAS Key Laboratory of Nanosystem and Hierarchical Fabrication, CAS Center for Excellence in Nanoscience, National Center for Nanoscience and Technology, Beijing 100190, China*
[4] *State Key Laboratory of Rare Earth Materials Chemistry and Applications, PKU-HKU Joint Laboratory in Rare Earth Materials and Bioinorganic Chemistry, Peking University, Beijing 100871, China*
§ *Chong Zhang, Jianhua Lu, and Falin Tian contributed equally to this work.*

Received: 1 January 2019 / **Revised:** 26 January 2019 / **Accepted:** 27 January 2019

ABSTRACT

Controlling the cellular interaction and internalization of polymer-modified nanoparticles (NPs) is of central importance to the development of promising nanomedicines. Here, we describe the use of synthetic polypeptides for NP surface coating and regulation of their cellular uptake behaviors by simply switching the conformation and anchoring orientation. Our results show that gold NPs (AuNPs) coated with a helical poly(γ-(2-(2-(2-methoxyethoxy)ethoxy)ethoxy)esteryl $_{L}$-glutamate) ($_{L}$-P(EG$_3$Glu)$_{50}$) from the C-terminus ((L-C)-AuNPs) exhibit greater zeta potential and more cellular uptake (2.0–5.5 fold higher) than those coated with the same polypeptide but anchored from the N-terminus ((L-N)-AuNPs), or from both the C- and N-terminus at a 1/1 molar ratio ((L-C/L-N)-AuNPs). A similar orientation-regulated cellular internalization pattern is observed in $_{D}$-P(EG$_3$Glu)$_{50}$ but not the unstructured $_{DL}$-P(EG$_3$Glu)$_{50}$-modified AuNPs, suggesting an important and universal role of the helix-derived macrodipole in cellular uptake. Moreover, this orientation-governed internalization is successfully reproduced in P(EG$_3$Glu)$_{50}$-coated gold nanorods (AuNRs), and applied to the design of doxorubicin-loaded polypeptide micelles. Simulation study offers time-resolved insights regarding the NP–membrane interactions and membrane remodeling. Thus, our study provides a delicate way of regulating the surface chemistry of NPs and the subsequent NP–cell interactions. Moreover, the results highlight the uniqueness of polypeptides in NP surface engineering, and urge a more careful consideration on the polymer orientation effect.

KEYWORDS

helix, orientation, polypeptides, cellular uptake, gold nanoparticles

1 Introduction

Numerous inorganic, organic, and lipid-based nanoparticles (NPs) have been developed for biomarker sensing [1, 2], diagnostic imaging [3–5], and therapeutic nanomedicines [6–9]. It has been widely accepted that the ultimate fate of the NPs in biological systems is governed by many physicochemical parameters. Often, a minor change in one of these parameters can lead to significant alteration of their biological outcomes both *in vitro* and *in vivo* [10–12]. Thus, identifying the critical structural characters, correlating them with the corresponding biological responses, and elaborating the mechanism of action, are of central importance. Taking the cellular internalization step as an example, many pioneering works have highlighted the pivotal role of the size [13–15], shape [16, 17], morphology [18–20], charge [21, 22], surface chemistry [22, 23], and rigidity [24] of different NPs.

Peptides and polypeptides are commonly used in the synthesis and modification of polymeric and inorganic nanoparticles [25–29]. One unique feature of peptides is their helical conformation that is more rigid than the unstructured coil. Previous works have shown that the helix of cell-penetrating peptides (CPPs) is essential to their membrane activity [30]. Moreover, the peptidic helix is known to have a macrodipole arising from the cumulative effect of the unidirectionally aligned individual peptide dipoles parallel to the helical axis [31]. This marcodipole can in turn generate an electrostatic field with a partial negative and positive pole near the C- and N-terminus, respectively [32, 33]. On substrate surfaces, controlling the orientation of peptide/polypeptide helix can regulate the self-assembly behaviors [34, 35] and implement unprecedented redox [36], piezoelectric [37], and electro-optical [38, 39] properties. Recently, we have demonstrated that when neutral or zwitterionic nonfouling polypeptides are coated on gold chips, both the helical conformation and the anchoring orientation can impact their anti-adsorption and anti-adhesion behaviors [40]. These unconventional findings inspire us to further study how the conformation and orientation of the synthetic polypeptide-modified NPs interact with cells, which is often overlooked and poorly understood. We hypothesize that the parallel-aligned (i.e. exclusively C- or N-terminal anchored) or antiparallel-orientated (i.e. both C- and N-terminal anchored) helical polypeptides on NPs may act cooperatively to

Address correspondence to Lingdong Sun, sun@pku.edu.cn; Xinghua Shi, shixh@nanoctr.cn; Hua Lu, chemhualu@pku.edu.cn

create surfaces with subtle alteration in macrodipole charges, and thus delicately regulate their cellular interaction and internalization behaviors.

2 Experiment section

2.1 Synthesis of thiol functioned poly(γ-(2-(2-(2-methoxyethoxy)ethoxy)ethoxy)esteryl glutamate) (P(EG$_3$Glu))

L-, D-, and DL-P(EG$_3$Glu)s were synthesized from the ring-opening polymerization of L-, D-, and DL-γ-(2-(2-(2-methoxyethoxy)ethoxy)ethoxy)esteryl glutamate-N-carboxyanhydride (DL-EG$_3$Glu-NCA), respectively [41]. Thiol functionalization of P(EG$_3$Glu)s at the C- and N-terminus was conducted according to our previous reports [40]. In this work, the right-handed helical L-P(EG$_3$Glu)s with the thiol at the C- and N-terminus were denoted as L-C and L-N, respectively; the equal molar mixture of L-C and L-N was named as L-C/L-N. Similarly, the left-handed helical D-P(EG$_3$Glu)s with the thiol at the C- and N-terminus were denoted as D-C and D-N, respectively; the equal molar mixture of D-C and D-N was named as D-C/D-N. Unstructured DL-P(EG$_3$Glu)s with the thiol at the C- and N-terminus were denoted as DL-C and DL-N, respectively; the equal molar mixture of DL-C and DL-N was named as DL-C/DL-N. Of note, the N-termini of L-C, D-C, and DL-C were capped by acetic anhydride as previously described [40].

2.2 Preparation of the polypeptide-coated gold NPs (AuNPs) and gold NRs (AuNRs)

Bare AuNPs with an average hydrodynamic size of ~ 16.9 nm were prepared by the citrate reduction of chloroauric acid according to previous protocols [42]. The cetyltrimethylammonium bromide (CTAB) stabilized AuNRs with an average aspect ratio of ~ 4.6 (length: 36.2 ± 3.4 nm, width: 7.8 ± 0.4 nm) were prepared following the well-established protocol of seed-mediated growth [43, 44]. The excess CTAB of AuNRs solution were removed by centrifuged at 12,000*g* for 20 min and then resuspended in water. Then, L-C, L-N, D-C, D-N, DL-C, and DL-N stock solutions were prepared by dissolving the corresponding polymers into water at 3.5 mg/mL; (D)L-C/(D)L-N were prepared by mixing an equal volume of (D)L-C and (D)L-N solutions. To prepare the polypeptide-modified AuNPs and AuNRs, each polymer solution (1.0 mL) was added to 50 mL bare AuNPs or CTAB stabilized AuNRs, followed by sonication for 30 min. The solutions were kept in dark and placed on an oscillator at room temperature for 12 h. The polypeptide-modified AuNPs and AuNRs were then purified by centrifugation/re-dispersion cycles in water three times (12,000*g*, 20 min) and re-dispersed in ultrapure water (1.0 mL). The concentrations of AuNPs and AuNRs were quantified by inductively coupled plasma mass spectrometry (ICP-MS).

2.3 Cellular uptake of polymer-coated AuNPs and AuNRs

HeLa cells (2.5×10^6) were seeded into culture dishes (100 mm) in 10 mL Dulbecco modified Eagle's medium (DMEM) supplemented with 10% fetal bovine serum (FBS) and 1% penicillin-streptomycin. After incubation at 37 °C for 24 h, the dishes were replaced with new culture media (10 mL) containing polypeptide-coated AuNPs or AuNRs at a concentration of 30 μM (n = 3). After another 6 or 12 h incubation, the cells were washed three times with sterilized phosphate buffered saline (PBS) and harvested using trypsin solution (1.0 mL). Cell numbers were determined using a hemocytometer. The cell pellets were collected by centrifugation at 1,000 rpm for 10 min to remove free NPs and digested with freshly prepared aqua regia (~ 5 mL). The total amount of intracellular gold was quantified using ICP-MS, and the resulting cellular uptake (Au (ng)/10^6 cells) of each sample was reported from the average of three independent measurements.

2.4 Cytotoxicity assays of polypeptide-coated AuNPs

HeLa cells were seeded in a 96-well plate at a density of 5,000 cells per well for 24 h before the experiment. The medium was aspirated and the cells were treated with culture media containing polypeptide-coated AuNPs at gradient concentrations (n = 3). After incubation for another 48 h, the relative cell viabilities were determined by the CellTiter-Blue Cell Viability Assay.

2.5 Transmission electron microscopy (TEM) images of the cellular uptake of (L-C)-AuNPs and (L-C)-AuNRs

HeLa cells with internalized nanoparticles were collected by centrifugation at 1,000 rpm for 10 min. The cell pellets were fixed with glutaraldehyde overnight. After serial dehydrations using 25%, 50%, 75%, 90%, and 100% acetone for 10 min in each step, the cell pellets were embedded in Epon resin, and sliced to a thickness of ~ 50–70 nm. The imagings of (L-C)-AuNPs and (L-C)-AuNRs locations in the cells were observed using TEM.

2.6 Synthesis of P(L-EG$_3$Glu)$_{50}$-b-PBLG$_{40}$ (E$_{50}$B$_{40}$) and PBLG$_{40}$-b-P(L-EG$_3$Glu)$_{50}$ (B$_{40}$E$_{50}$) block copolymers

P(L-EG$_3$Glu)$_{50}$-b-PBLG$_{40}$: A solution of hexamethyldisilazane (HMDS) HMDS (12.5 μL × 0.5 M, 1.0 eq.) was added to a stirring solution of L-EG$_3$Glu-NCA (100 mg, 0.32 mmol, 50 eq.) in dimethylformamide (DMF) (2.0 mL) in a glovebox at room temperature. After the complete consumption of L-EG$_3$Glu-NCA (monitored by FT-IR), a solution of γ-benzyl-L-glutamate-N-carboxyanhydride (BLG-NCA) (68.4 mg, 0.26 mmol, 40 eq.) in DMF (1.0 mL) was added. After another 24 h reaction, acetic anhydride (20 eq.) was added to cap the terminal amine groups. The crude block copolymer was then isolated by precipitation out using diethyl ether. After sonication for 5 min in diethyl ether, the product P(L-EG$_3$Glu)$_{50}$-b-PBLG$_{40}$ was collected by centrifugation and dried under vacuum.

PBLG$_{40}$-b-P(L-EG$_3$Glu)$_{50}$: PBLG$_{40}$-b-P(L-EG$_3$Glu)$_{50}$ was synthesized by following a similar procedure as described above, except for a inversed addition sequence of the two monomers: BLG-NCA was polymerized first, followed by L-EG$_3$Glu-NCA.

For clarity purpose P(L-EG$_3$Glu)$_{50}$-b-PBLG$_{40}$ and PBLG$_{40}$-b-P(L-EG$_3$Glu)$_{50}$ were denoted as E$_{50}$B$_{40}$ and B$_{40}$E$_{50}$, respectively.

2.7 Fabrication of DOX-loaded polymeric micelles

Doxorubicin hydrochloride (DOX·HCl) (2.5 mg) was dispersed in tetrahydrofuran (THF) (1.5 mL) and neutralized by TEA (3.0 μL). The designated block polymer (5.0 mg) in THF (1.0 mL) was added into the free DOX solution and stirred for 3 h. Next, distilled water (500 μL) was added dropwise to the above DOX/polymer mixture under vigorous stirring. The crude DOX-loaded polypeptide micelles were stirred overnight and purified by dialysis against distilled water (MWCO 3,500) at room temperature for 3 days. The deionized water was replaced every 10 h. To measure the DOX loading in the micelle, a solution of DOX-loaded polypeptide micelle was diluted with DMF (DMF/H_2O, 9/1, v/v) and sonicated for 10 min. The fluorescence intensity at 587 nm (excitation at 479 nm) was recorded, and the concentration of DOX loading in triethylamine (TEA) micelle was determined based on the standard curve of free DOX in DMF/H_2O (9/1, v/v). All the experiments were operated in dark.

2.8 Cell uptake of DOX-loaded polymeric micelles

HeLa cells (1.5×10^5) were initially seeded in a 24-well plate and grown at 37 °C for 24 h. Then, the cells were treated with free DOX or DOX-loaded polymeric micelles in fresh medium at a DOX concentration of 100 μM for 1.0 h. The cells were washed with PBS (twice), digested by trypsin (200 μL) for 5 min, and quenched with the PBS (500 μL) dilution. The HeLa cell pellets were collected by centrifugation at 1,000 rpm for 5 min and then dispersed in PBS

(0.6 mL). The cellular uptake of DOX-loaded polypeptide micelles was characterized using flow cytometry.

2.9 Cytotoxicity assays of DOX-loaded polypeptide micelles

HeLa cells were first seeded in a 96-well plate at a density of 5,000 cells per well. Then, the cells were treated with free DOX or DOX-loaded polypeptide micelles in fresh medium at gradient DOX concentrations of 150, 100, and 50 μM (n = 3), respectively. 1 h later, the medium was aspirated and the cells were washed twice with PBS before another 48 h incubation. The relative cell viabilities were detected using CellTiter-Blue Cell Viability Assay.

2.10 Molecular simulation

A CG model and dissipative particle dynamics (DPD) method were used to elucidate the endocytosis mechanism of the AuNPs and AuNRs with different surface modifications. To simplify the system, we constructed a model comprising a piece of cellular membrane, NP/NR with different kinds of ligands and water. The cellular membrane is formed by an assembly of lipids and receptors as a stable bilayer structure. Each lipid/receptor molecule comprised 13 DPD beads like Groot and Rabone DPD model [45]. The NP/NR is formed by particle beads arranged on a face-centered cubic lattice to prevent other beads' insertion and constrained to move as a rigid body during the simulations [46]. The ligands are connected on the surface of the NP/NR directly. In order to mimic the receptor–ligand interaction, a modified soft Lennard-Jones (LJ) potential was used during the NP/NR–membrane interaction simulations. The dipole interaction was represented by an electrostatic interactions in the simulation. The bonded interaction between neighboring beads of the lipid, receptor, and ligand was described by a harmonic spring force. The stiffness of the lipid membrane is constrained by a three-body bond angle potential. The interaction between each pair of DPD beads is governed by Newton's equation of motion $dv_{ij}/dt = F_{ij}/m$ and the total force F_{ij} applied on each bead i due to bead j is given as a sum of six terms, i.e., conservative force F_{ij}^{C}, dissipative force F_{ij}^{D}, random force F_{ij}^{R}, bond force F_{ij}^{B} (including the harmonic bond force and bond angle force), the electrostatic force F_{ij}^{E} converted from the dipole of the ligand and the LJ interaction between ligands and receptors. The details of the setup of the system and the interaction potential are listed in the Electronic Supplementary Material (ESM).

The simulation box is a cube of size $100r_c \times 100r_c \times 80r_c$ with periodic boundary condition applied three directions. There are total 2,400,000 beads in the simulation box to keep the particle density close to 3.0. To avoid the distribution of the nanoplate to the equilibrium state of a pure membrane, a long time (~ 200 ns) equilibrium simulation was preformed when the NP/NR was placed near the membrane surface. All simulations in this work are carried out by using the modified soft package Lammps (31 Mar 2017).

3 Results and discussion

3.1 Preparation of polypeptide-coated AuNPs and AuNRs

L-, D-, or DL-P(EG$_3$Glu)s bearing a thiol group at either the C- or N-terminus for AuNP anchoring were synthesized by following our previous report (Fig. 1) [40]. All the synthetic polypeptides shared a similar degree of polymerization (DP) ~ 50 with narrow dispersities ($Đ$) below 1.10 (Fig. S1 and Table S1 in the ESM). As expected, the three L-configurated (L-C, L-N, and L-C/L-N) and the three D-configurated (D-C, D-N, and D-C/D-N) polypeptides all depicted a typical α-helical conformation with the helicity higher than 90% (Fig. 2(a)). The L- and D-P(EG$_3$Glu)s gave an completely opposite shape of circular dichroism (CD) peaks, indicating the two types of polypeptides had right- and left-handed helix, respectively. By contrast, none of the racemic DL-C, DL-N, and DL-C/DL-N gave an ordered conformation according to the CD spectra (Fig. 2(a)).

Next, the polypeptides were grafted to bare AuNPs at room temperature via the Au–S bond. The strong amide I stretching at 1,650 cm^{-1} and amide II stretching bands at 1,548 cm^{-1} in the FT-IR spectra of polypeptide-coated AuNPs reconfirmed the α-helical secondary structure of L-C and L-N on the AuNP surface (Fig. 2(b)) [47]. No shift was observed in the surface plasmon resonance peak (λ_{spr}, ~ 521 nm, Fig. 2(c)) of AuNPs, an indication of no aggregation after the polymer modification. The high colloidal stability of (L-C)-AuNPs and (DL-C)-AuNPs was further evidenced by the representative TEM images showing monodispersed and spherical particles (Fig. S2 in the ESM). The nonfouling behaviors of the polypeptide-coated AuNPs were evaluated by studying the protein adsorption-induced NP aggregation. Lysozyme and fibrinogen, two commonly used model proteins for surface antifouling tests, were added to various AuNPs [48, 49]. The protein adsorption of the AuNPs was reflected by the shift in the surface plasmon absorption ($\Delta\lambda_{spr}$) [50]. As shown in Figs. 2(d) and 2(e), after the addition of the protein solution, the λ_{spr} of bare AuNPs showed a drastic red shift, in sharp contrast to the minor shifts for polypeptide-coated AuNPs, underscoring again the high *in vitro* stability of the polypeptide-coated AuNPs against protein adsorption.

The hydrodynamic sizes of all the bare and polymer-modified AuNPs were measured by dynamic light scattering (DLS) and shown in Table 1. After the polypeptide modification, the parallel aligned (L-C)-AuNPs and (L-N)-AuNPs displayed a similar hydrodynamic size ~ 32 nm and a surface grafting density of 120 chains per AuNP (calculated by thermogravimetric analysis (TGA), Fig. S3 in the ESM). In contrast, the anti-parallel orientated (L-C/L-N)-AuNPs gave a relative higher hydrodynamic size ~ 37 nm and a greater grafting density of 136 chains per AuNP. This higher grafting density of (L-C/L-N)-AuNPs

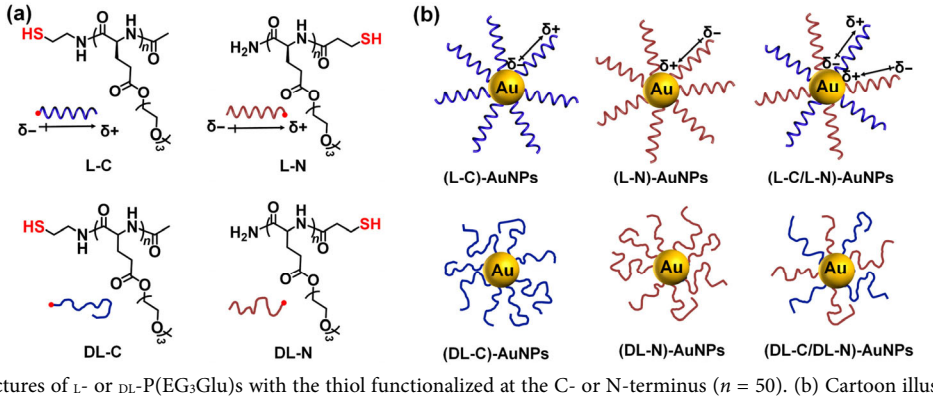

Figure 1 (a) Chemical structures of L- or DL-P(EG$_3$Glu)s with the thiol functionalized at the C- or N-terminus (n = 50). (b) Cartoon illustration of AuNPs modified with P(EG$_3$Glu)s adapting different secondary structures and/or anchoring orientations. Arrows indicate the moment of the helix macrodipole. δ+ and δ− indicate the partially positive and negative dipole ends of the helices, respectively.

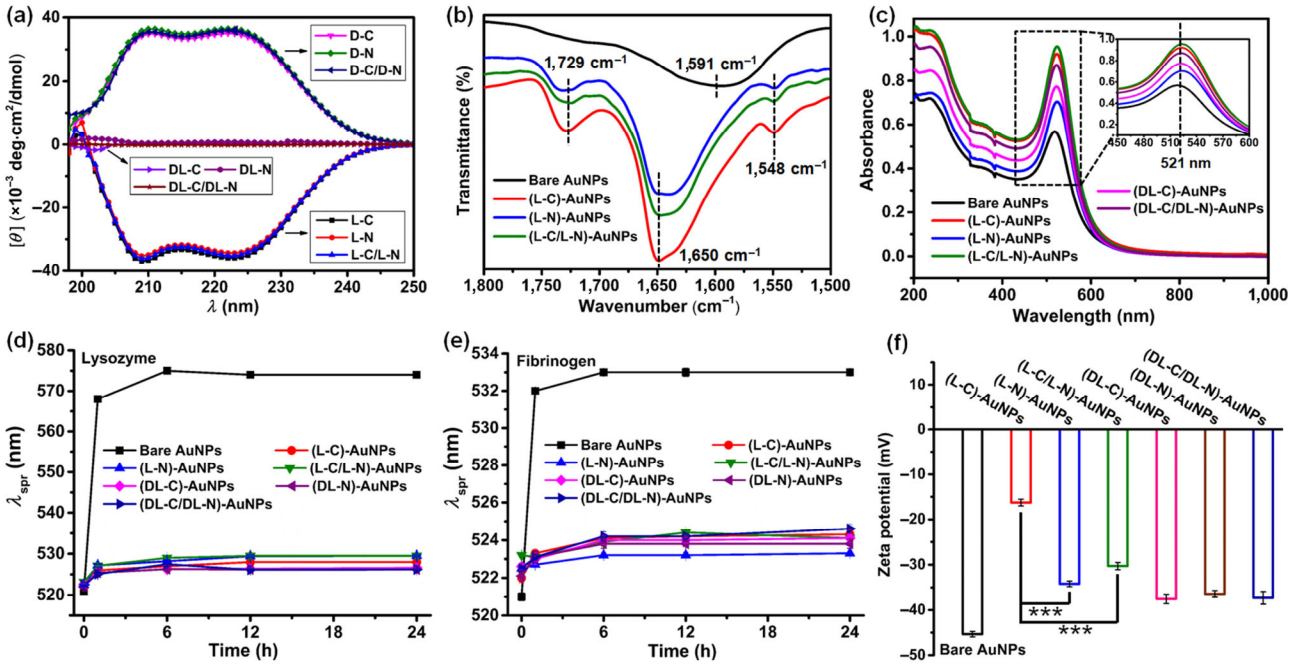

Figure 2 (a) CD spectra of L-, D-, or DL-P(EG$_3$Glu)s bearing a thiol group at either the C- or N-terminus. (b) FT-IR spectra of the bare and polypeptide-coated AuNPs. (c) UV–Vis spectra of AuNPs coated with different polypeptides (inset: the zoom-in view of the spectra from 450 to 600 nm). (d) and (e) Shift of the peak of the surface plasmon resonance wavelength (λ_{spr}) of different polypeptide-coated AuNPs as a function of time in (d) lysozyme and (e) fibrinogen, respectively. (f) Zeta potential of the bare and polypeptide-coated AuNPs in H_2O. All of the data are represented as the means ± S.D. The p value (*p < 0.01, **p < 0.001 and ***p < 0.0001) is calculated by t-test.

Table 1 Hydrodynamic size[a] and grafting density[b] of various polypeptide-coated AuNPs

	Bare AuNPs	(L-C)-AuNPs	(L-N)-AuNPs	(L-C/L-N)-AuNPs	(DL-C)-AuNPs	(DL-N)-AuNPs	(DL-C/DL-N)-AuNPs
Size (nm)	16.9 ± 1.3	32.2 ± 1.1	32.8 ± 0.7	36.9 ± 0.9	25.9 ± 1.1	27.4 ± 1.1	26.8 ± 0.8
Grafting density (chains/nm^2)	—	0.148 ± 0.005	0.15 ± 0.003	0.17 ± 0.004	0.123 ± 0.005	0.13 ± 0.005	0.126 ± 0.004
Ligand density (chains/AuNPs)	—	119 ± 4	121 ± 2	136 ± 3	99 ± 4	104 ± 4	101 ± 3

[a]measured by DLS; [b]calculated from the weight loss in TGA.

was likely due to the cancelling of the repulsive force derived from the dipole moment, a phenomenon we previously observed on flat gold substrate [40]. Moreover, the unstructured P(EG$_3$Glu)s modified AuNPs, namely, (DL-C)-AuNPs, (DL-N)-AuNPs, and (DL-C/DL-N)-AuNPs showed smaller hydrodynamic sizes (~ 26–27 nm) and lower grafting densities (~ 99–104 chains per AuNP) relative to the former three helical polypeptide-modified AuNPs (Table 1). Overall, the rigid helical polypeptides were more favored for surface grafting than the unstructured polypeptide analogues, in good consistency with our conclusions previously reported. Figure 2(f) showed the zeta potential of the bare and polypeptide-coated AuNPs in H_2O. The bare AuNPs showed the most negative zeta potential ~ −45 mV due to citrate-stabilization, which became less negative after the replacement of citrate with polypeptide. Interestingly, (L-C)-AuNPs gave the least negative zeta potential ~ −16 mV whereas all other AuNPs were comparable (~ −30–−37 mV). Given the comparable grafting density of (L-C)-AuNPs and (L-N)-AuNPs, we attributed the relative more positive zeta potential of the former to the multivalent accumulation of the partial positive macrodipole at the outer layer surface.

3.2 Cellular uptake of polypeptide-coated AuNPs

Next, the cellular internalization behaviors of different polypeptide-coated AuNPs were investigated by using HeLa cells and measured by ICP-MS. We first examined the orientation effect in the right-handed helical polypeptides (L-configuration). When the helical L-P(EG$_3$Glu)$_{50}$ was anchored on the surface of AuNPs in different orientations, the most remarkable feature we noticed was the significantly higher amount of cellular internalization of (L-C)-AuNPs (~ 5.5 and 2.1 fold higher, respectively) compared to both (L-N)-AuNPs and (L-C/L-N)-AuNPs (Fig. 3(a)). Moreover, a clear time-dependent increase in the internalization level was seen for all samples (Fig. 3(a)). Interestingly, this orientation effect was not detected for AuNPs coated with the unstructured DL-P(EG$_3$Glu)$_{50}$. More specifically, (DL-C)-AuNPs, (DL-N)-AuNPs, and (DL-C/DL-N)-AuNPs gave no statistical difference in terms of the cellular internalization at both 6 and 12 h incubation (Fig. 3(b)). When directly comparing the cellular uptake level of (L-C)-AuNPs with (DL-C)-AuNPs, the former was ~ 2.4 folder higher than the latter (Fig. 3(b)). The results indicated that the orientation effect existed only in those helical polypeptide-modified AuNPs, implying a role of the macrodipole. Notably, the cellular internalization level of different polypeptide-modified AuNPs showed a good correlation with the zeta-potential described in Fig. 2(f). Namely, (L-C)-AuNPs, the least negative in zeta potential among all tested groups, gave the highest level of cellular internalization. This phenomenon was to some degree similar to the promoted cellular adhesion of polyvalent choline phosphate (CP) in relative to the charge-inversed polyvalent phosphatidyl choline (PC) [51]. To further understand the orientation effect, we also generated AuNPs coated with the left-handed helical D-P(EG$_3$Glu)$_{50}$ (Table S2 in the ESM). Again, the C-terminal anchored (D-C)-AuNPs gave a higher level of cellular internalization than the N-terminal anchored (D-N)-AuNPs and the anti-parallel aligned

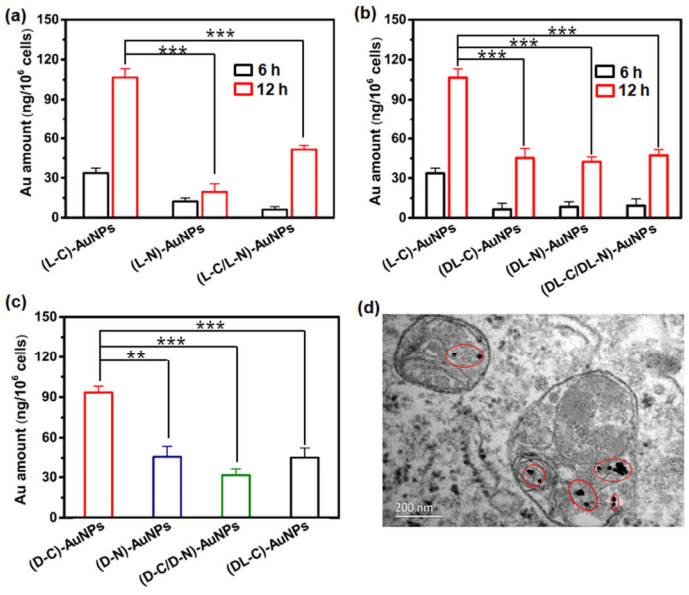

Figure 3 Cellular uptake of the polypeptide-coated AuNPs. (a) The internalization level of AuNPs coated with the right-handed helical L-P(EG_3Glu)$_{50}$ anchoring from different orientations after 6 and 12 h incubation. (b) The internalization level of AuNPs modified with the unstructured DL-P(EG_3Glu)$_{50}$ anchoring from different orientations after 6 and 12 h incubation, compared with that of (L-C)-AuNPs under the same condition. (c) The internalization level of AuNPs modified with the left-handed helical D-P(EG_3Glu)$_{50}$ anchoring from different orientations after 12 h incubation. (d) Representative TEM image of the cell sections after the internalization of (L-C)-AuNPs after 12 h incubation. The AuNPs in 30 μM were incubated with cells for 6 or 12 h at 37 °C in normal medium with 10% FBS, unless otherwise specified. All of the data are represented as the means ± S.D. The p value (*p < 0.01, **p < 0.001 and ***p < 0.0001) is calculated by t-test.

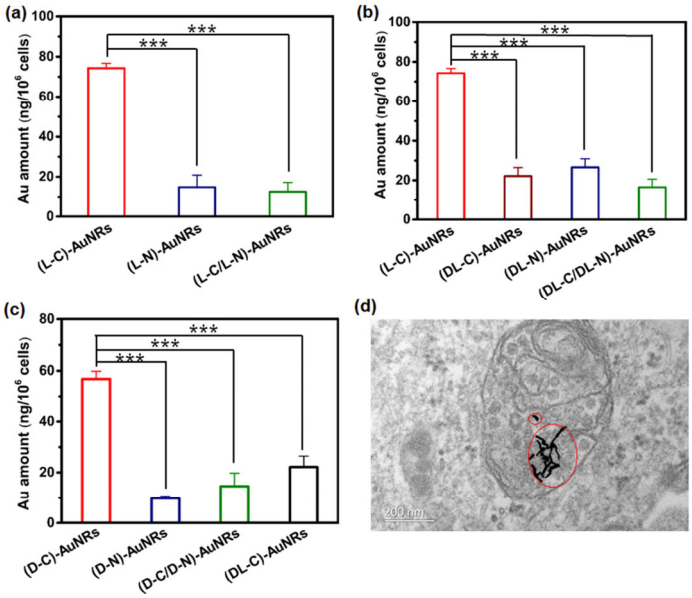

Figure 4 Cellular uptake of the polypeptide-coated AuNRs. (a) The internalization level of AuNRs coated with the right-handed helical L-P(EG_3Glu)$_{50}$ anchoring from different orientations. (b) The internalization level of AuNRs modified with the unstructured DL-P(EG_3Glu)$_{50}$ anchoring from different orientations, compared with that of (L-C)-AuNRs under the same condition. (c) The internalization level of AuNRs modified with the left-handed helical D-P(EG_3Glu)$_{50}$ anchoring from different orientations. (d) Representative TEM image of the cell sections after the internalization of (L-C)-AuNRs. The AuNRs in 30 μM were incubated with cells for 12 h at 37 °C in normal medium with 10% FBS, unless otherwise specified. All of the data are represented as the means ± S.D. The p value (*p < 0.01, **p < 0.001 and ***p < 0.0001) is calculated by t-test.

(D-C/D-N)-AuNPs (Fig. 3(c)). The level of internalization was comparable for (D-C)-AuNPs and (L-C)-AuNPs at 12 h incubation (Figs. 3(a) and 3(c)), implying that the handedness of the helix was not crucial to the internalization in this particular case. One possible reason for this handedness-independence might be the long nonfouling EG_3 side chain, which masked the handed character of the backbone. It is also worth mentioning that the N-termini of the L-C, D-C, and DL-C polypeptides were all capped with acetic anhydride, which ruled out the possibility of the N-terminal amine pronation. TEM studies of the (L-C)-AuNPs treated Hela cells found the NPs were majorly trapped in endolysosomal vesicles, suggesting an endocytosis pathway (Fig. 3(d)) [12, 52]. No obvious cellular toxicity was observed for all the polypeptide-coated AuNPs (Fig. S4 in the ESM) in a wide range of concentrations up to 560 μM, including the highly internalizable (L-C)-AuNPs. The neutral charge, excellent biocompatibility, and high level of internalization made (L-C)-AuNPs particularly suitable for situations where the use of cytotoxic polycation for cell uptake promotion are not allowed.

3.3 Cellular uptake of AuNRs

To test whether the orientation effect was also applicable to other NPs, particularly those with different shapes, AuNRs (Fig. S5 and Table S3 in the ESM) were prepared and modified with the same polypeptides described above. The cell internalization behaviors of those polypeptide-coated AuNRs were studied in a similar way and presented in Fig. 4. To summarize, the polypeptide-coated AuNPs and AuNRs followed a very similar cell internalization pattern. Briefly, (L-C)-AuNRs and (D-C)-AuNRs, the two AuNRs coated with the parallel aligned helical P(EG_3Glu)$_{50}$ from the C-terminus, showed the highest internalization level compared to all other groups including (L-N)-AuNRs, (L-C/L-N)-AuNRs (Fig. 4(a)), (DL-C)-AuNRs, (DL-N)-AuNRs, (DL-C/DL-N)-AuNRs (Fig. 4(b)), (D-N)-AuNRs, and (D-C/D-N)-AuNRs (Fig. 4(c)). TEM studies of the (L-C)-AuNRs-treated Hela cells (Fig. 4(d)) showed a similar endocytosis mechanism as previously observed in Fig. 3(d).

3.4 Cellular uptake of polymer micelles

To further examine the generality of the orientation effect, we moved on to test the cellular internalization of micelles from self-assembled amphiphilic block copolypeptides. As shown in Fig. 5(a), $B_{40}E_{50}$ was prepared by sequential polymerization of BLG-NCA and EG_3Glu-NCA, respectively; by contrast, the analogue block copolymer $E_{50}B_{40}$ was prepared by inversing the sequence in monomer feeding (Fig. S6 in the ESM). The two polymers showed comparable molecular weights and dispersities as determined by both size exclusion chromatography (SEC) and ^{1}H NMR spectroscopy (Figs. S7–S9 and Table S4 in the ESM) analysis. Both block copolymers were used to self-assemble in water to form micelles, which were subsequently loaded with a chemotherapy drug DOX. TEM studies of the DOX-loaded $B_{40}E_{50}$ and $E_{50}B_{40}$ micelles exhibited similar sizes of ~ 115 nm (Fig. 5(b)). Fluorescence spectroscopy determined that both micelles had a similar amount of DOX encapsulated. Thus, the polypeptide orientation became the only major variation, with all other structural parameters keeping similar or the same. If the AuNPs, AuNRs and the polymeric micelles share a similar orientation effect, one would expect that both the internalization and cellular toxicity of the DOX-loaded $B_{40}E_{50}$ (partial positive macrodipole at the outer layer) should be higher than those of $E_{50}B_{40}$ (partial negative macrodipole at the outer layer). As shown in Fig. 5(c), DOX-loaded $B_{40}E_{50}$ showed a significantly increase in zeta potential than DOX-loaded $B_{40}E_{50}$. Furthermore, HeLa cells incubated with the DOX-loaded $B_{40}E_{50}$ micelle showed enhanced cellular uptake in relative to the DOX-loaded $E_{50}B_{40}$ micelle, determined by flow cytometry (Fig. 5(d)). Consistently, viability assay indicated that the DOX-loaded $B_{40}E_{50}$ was more cytotoxic than the DOX-loaded $E_{50}B_{40}$ (Fig. 5(e)). No toxicity was observed for both $E_{50}B_{40}$ and $B_{40}E_{50}$ micelles without DOX (Fig. S10 in the ESM). Together, the results shown in the polymeric micelles echoed the

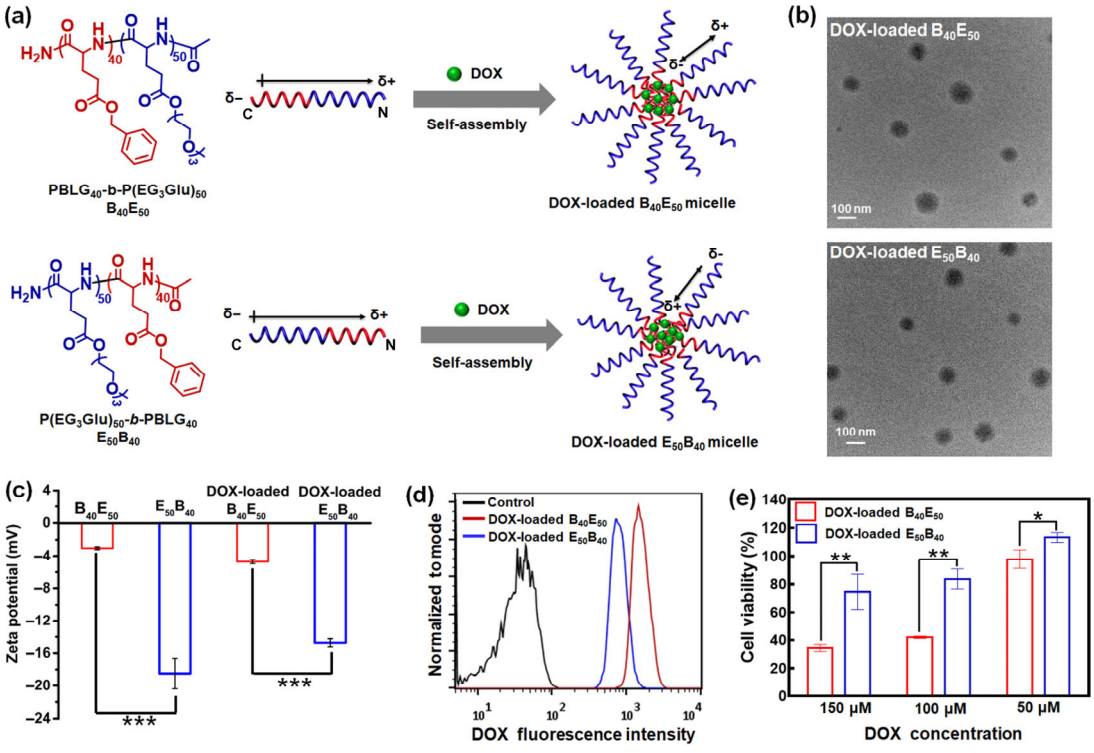

Figure 5 Cellular uptake of DOX-loaded $E_{50}B_{40}$ and $B_{40}E_{50}$ polypeptide micelles. (a) Chemical structure of two amphiphilic block copolypeptides $B_{40}E_{50}$ and $E_{50}B_{40}$, and the schematic illustration of the micelle compositions. (b) TEM images of the DOX-loaded $E_{50}B_{40}$ and $B_{40}E_{50}$ micelles. Scale bar = 100 nm. (c) Zeta potential of DOX-loaded $E_{50}B_{40}$ and $B_{40}E_{50}$ micelles in H_2O. (d) Flow cytometric histogram profiles of the HeLa cells incubated with the DOX-loaded $E_{50}B_{40}$ or $B_{40}E_{50}$ micelles at 100 μM. (e) Relative cell viability of HeLa cells incubated with DOX-loaded $E_{50}B_{40}$ or $B_{40}E_{50}$ micelles; the cells were treated with the samples for 1 h, and incubated with fresh medium for another 48 h. All of the data are represented as the means ± S.D. The p value (*$p < 0.01$, **$p < 0.001$ and ***$p < 0.0001$) is calculated by t-test.

previous phenomenon observed in AuNPs and AuNRs, which once again highlighted the important role of the helical macrodipole orientation in cellular uptake.

3.5 Computer simulation

To elucidate the mechanism of the helical orientation effect on AuNPs cellular uptake, we conducted DPD simulations by using a dipalmitoylphosphatidylcholine (DPPC) lipid bilayer model. For simplicity purpose, the helical and unstructured polypeptides were modeled as rigid and soft chains, respectively (Table S5 and Fig. S11 in the ESM). The macrodipole of the helix was represented with a positive and negative charge bead at the N and C chain end, respectively. Next, we constructed prototype models of NPs with the helical polypeptide anchored from C-terminus ((Helix-C)-AuNPs), N-terminus ((Helix-N)-AuNPs), and both C-/N-termini ((Helix-C/Helix-N)-AuNPs), respectively (Fig. S11 in the ESM; of note, the handedness of the helix was not considered here). Accordingly, coil-AuNPs, constructed as NPs modified with soft chains and without charged beads, were used here as a model to represent all unstructured DL-type polypeptide-modified AuNPs (Fig. S11 in the ESM). The simulation setup was similar to that used in earlier study (see Experimental Section and Fig. S11 in the ESM) [17, 53, 54]. Briefly, a receptor–NP binding universal to all NPs was introduced as the initial driving force for receptor-mediated endocytosis. Initially, the NPs were positioned in close proximity above the surface of a bilayer; the NPs were then bonded onto the membrane receptors through a soft LJ potential and electronic interaction (see Experimental Section). As the NPs adhered to the membrane, receptor clustering and membrane wrapping took place to pull the NPs inside (Fig. 6(a) in the ESM).

For (Helix-C)-AuNPs, the NPs were wrapped and internalized rapidly (Figs. 6(b) and 6(c)). The reason was probably that the long range electronic attractive force between the ligand and receptor

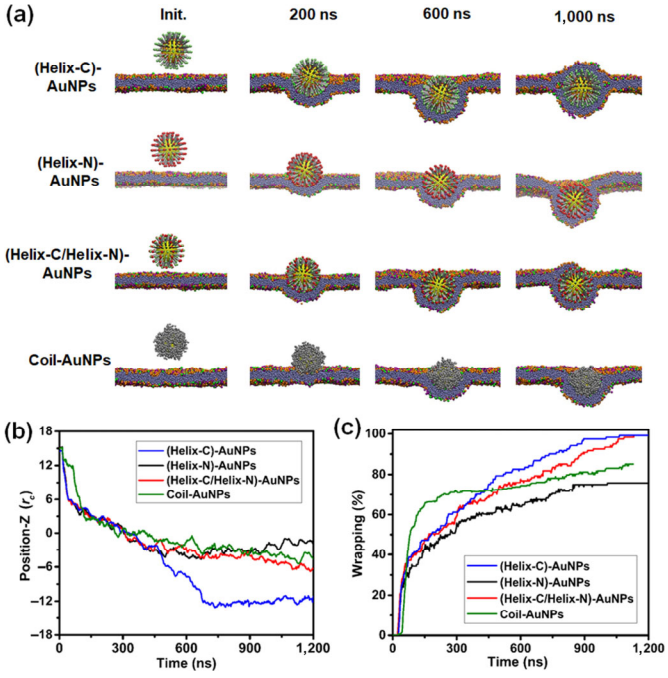

Figure 6 Simulation of the interactions between lipid membrane and spherical NPs with different surface modifications. (a) Snapshots of time-dependent interactions between different spherical NPs and membranes. For clarity, the solvent (water) molecules are made invisible. (b) and (c) Time evolution of (b) the position of the NP relative to the middle line of the membrane and (c) the NP–receptor binding ratio (percentage of wrapping). The distance values for determining the NP–receptor binding is selected within a distance of $0.7r_c$.

attracted more receptors around the NPs, which helped the bending of the membrane and finally the successful internalization of the NPs. For (Helix-N)-AuNPs, the NPs were seen to adhere onto the

membrane but with impeded wrapping owing to strong electrostatic repulsion between the NPs and the membrane (Fig. 6). For (Helix-C/Helix-N)-AuNPs, the wrapping was slower than (Helix-C)-AuNPs but faster than (Helix-N)-AuNPs at the late stage (Fig. 6(c)). Interestingly, for the soft coil-AuNPs without the helical macrodipole, we observed a fast ligand–receptor binding in the early stage but a slower membrane curving compared to (Helix-C)-AuNPs. We reasoned that although coil-AuNPs had the largest ligand–receptor binding in the early stage, the deformability and the lack of dipole interaction made the soft unstructured polypeptide less potent in attracting lipid for NP wrapping. Similar patterns were observed in the simulation of different polypeptide-modified AuNRs (Fig. S12 in the ESM).

4 Conclusions

The helix of polypeptides have shown profound impact to their biological outcomes, including the nonfouling property and immunogenicity as demonstrated recently [33, 40, 55]. In this work, the effect of polypeptide conformation and anchoring orientation were systematically investigated using inorganic AuNPs, AuNRs, and polymeric micelles. Our results revealed greater cellular uptake (2.0–5.5 fold higher) of (L-C)-AuNPs than (L-N)-AuNPs and (L-C/L-N)-AuNPs. A similar orientation-regulated cell internalization pattern was observed in $_{D}$-P(EG$_3$Glu)$_{50}$ but not the unstructured $_{DL}$-P(EG$_3$Glu)$_{50}$-modified AuNPs, suggesting an important and universal role of the macrodipole of peptidice helices in cellular uptaking. Moreover, this orientation-governed cellular internalization was successfully reproduced in P(EG$_3$Glu)$_{50}$-coated AuNRs and DOX-loaded polypeptide micelles. Simulation study offered time-resolved insights regarding the NP–membrane interactions and subsequent membrane remodeling. Thus, our study provided a delicate way of regulating the surface chemistry of NPs and the subsequent NP–cell interactions. Moreover, this work highlighted the uniqueness of polypeptides in surface engineering, and urged a more careful consideration on the polymer orientation for NP modification.

Acknowledgments

Financial supports from the National Key Research and Development Program of China (No. 2016YFA0201400) and the National Natural Science Foundation of China (No. 21722401) are gratefully acknowledged.

Electronic Supplementary Material: Supplementary material (materials and instrumentation; SEC and ^{1}H NMR spectra of synthesized polymers; TEM images, TGA curves, viability assay and DLS characterization of polypeptide-coated AuNPs and AuNRs; cytotoxicity assay of polymer micelles and details for simulation method and model) is available in the online version of this article at https://doi.org/10.1007/s12274-019-2319-6.

References

[1] Saha, K.; Agasti, S. S.; Kim, C.; Li, X. N.; Rotello, V. M. Gold nanoparticles in chemical and biological sensing. *Chem. Rev.* **2012**, *112*, 2739–2779.

[2] Chinen, A. B.; Guan, C. M.; Ferrer, J. R.; Barnaby, S. N.; Merkel, T. J.; Mirkin, C. A. Nanoparticle probes for the detection of cancer biomarkers, cells, and tissues by fluorescence. *Chem. Rev.* **2015**, *115*, 10530–10574.

[3] Kim, D.; Kim, J.; Park, Y. I.; Lee, N.; Hyeon, T. Recent development of inorganic nanoparticles for biomedical imaging. *ACS Cent. Sci.* **2018**, *4*, 324–336.

[4] Dong, H.; Du, S. R.; Zheng, X. Y.; Lyu, G. M.; Sun, L. D.; Li, L. D.; Zhang, P. Z.; Zhang, C.; Yan, C. H. Lanthanide nanoparticles: From design toward bioimaging and therapy. *Chem. Rev.* **2015**, *115*, 10725–10815.

[5] Lane, L. A.; Qian, X. M.; Nie, S. M. SERS nanoparticles in medicine: From label-free detection to spectroscopic tagging. *Chem. Rev.* **2015**, *115*, 10489–10529.

[6] Björnmalm, M.; Thurecht, K. J.; Michael, M.; Scott, A. M.; Caruso, F. Bridging bio-nano science and cancer nanomedicine. *ACS Nano* **2017**, *11*, 9594–9613.

[7] Pelaz, B.; Alexiou, C.; Alvarez-Puebla, R. A.; Alves, F.; Andrews, A. M.; Ashraf, S.; Balogh, L. P.; Ballerini, L.; Bestetti, A.; Brendel, C. et al. Diverse applications of nanomedicine. *ACS Nano* **2017**, *11*, 2313–2381.

[8] Yang, X.; Yang, M. X.; Pang, B.; Vara, M.; Xia, Y. N. Gold nanomaterials at work in biomedicine. *Chem. Rev.* **2015**, *115*, 10410–10488.

[9] Li, S. X.; Feng, X. R.; Wang, J. X.; He, L.; Wang, C. X.; Ding, J. X.; Chen, X. S. Polymer nanoparticles as adjuvants in cancer immunotherapy. *Nano Res.* **2018**, *11*, 5769–5786.

[10] Behzadi, S.; Serpooshan, V.; Tao, W.; Hamaly, M. A.; Alkawareek, M. Y.; Dreaden, E. C.; Brown, D.; Alkilany, A. M.; Farokhzad, O. C.; Mahmoudi, M. Cellular uptake of nanoparticles: Journey inside the cell. *Chem. Soc. Rev.* **2017**, *46*, 4218–4244.

[11] Zhao, F.; Zhao, Y.; Liu, Y.; Chang, X. L.; Chen, C. Y.; Zhao, Y. L. Cellular uptake, intracellular trafficking, and cytotoxicity of nanomaterials. *Small* **2011**, *7*, 1322–1337.

[12] Verma, A.; Stellacci, F. Effect of surface properties on nanoparticle–cell interactions. *Small* **2010**, *6*, 12–21.

[13] Jiang, W.; Kim, B. Y. S.; Rutka, J. T.; Chan, W. C. W. Nanoparticle-mediated cellular response is size-dependent. *Nat. Nanotechnol.* **2008**, *3*, 145–150.

[14] Tang, L.; Yang, X. J.; Yin, Q.; Cai, K. M.; Wang, H.; Chaudhury, I.; Yao, C.; Zhou, Q.; Kwon, M.; Hartman, J. A. et al. Investigating the optimal size of anticancer nanomedicine. *Proc. Natl. Acad. Sci. USA* **2014**, *111*, 15344–15349.

[15] Mosquera, J.; García, I.; Liz-Marzán, L. M. Cellular uptake of nanoparticles versus small molecules: A matter of size. *Acc. Chem. Res.* **2018**, *51*, 2305–2313.

[16] Chithrani, B. D.; Chan, W. C. W. Elucidating the mechanism of cellular uptake and removal of protein-coated gold nanoparticles of different sizes and shapes. *Nano Lett.* **2007**, *7*, 1542–1550.

[17] Li, Y.; Kröger, M.; Liu, W. K. Shape effect in cellular uptake of PEGylated nanoparticles: Comparison between sphere, rod, cube and disk. *Nanoscale* **2015**, *7*, 16631–16646.

[18] Verma, A.; Uzun, O.; Hu, Y. H.; Hu, Y.; Han, H. S.; Watson, N.; Chen, S.; Irvine, D. J.; Stellacci, F. Surface-structure-regulated cell-membrane penetration by monolayer-protected nanoparticles. *Nat. Mater.* **2008**, *7*, 588–595.

[19] Xue, J. X.; Guan, Z.; Lin, J. P.; Cai, C. H.; Zhang, W. J.; Jiang, X. Q. Cellular internalization of rod-like nanoparticles with various surface patterns: Novel entry pathway and controllable uptake capacity. *Small* **2017**, *13*, 1604214.

[20] Mochida, Y.; Cabral, H.; Miura, Y.; Albertini, F.; Fukushima, S.; Osada, K.; Nishiyama, N.; Kataoka, K. Bundled assembly of helical nanostructures in polymeric micelles loaded with platinum drugs enhancing therapeutic efficiency against pancreatic tumor. *ACS Nano* **2014**, *8*, 6724–6738.

[21] Hühn, D.; Kantner, K.; Geidel, C.; Brandholt, S.; De Cock, I.; Soenen, S. J. H.; Rivera_Gil, P.; Montenegro, J. M.; Braeckmans, K.; Müllen, K. et al. Polymer-coated nanoparticles interacting with proteins and cells: Focusing on the sign of the net charge. *ACS Nano* **2013**, *7*, 3253–3263.

[22] Hauck, T. S.; Ghazani, A. A.; Chan, W. C. W. Assessing the effect of surface chemistry on gold nanorod uptake, toxicity, and gene expression in mammalian cells. *Small* **2008**, *4*, 153–159.

[23] Wang, X. Y.; Wang, M. Z.; Lei, R.; Zhu, S. F.; Zhao, Y. L.; Chen, C. Y. Chiral surface of nanoparticles determines the orientation of adsorbed transferrin and its interaction with receptors. *ACS Nano* **2017**, *11*, 4606–4616.

[24] Sun, J. S.; Zhang, L.; Wang, J. L.; Feng, Q.; Liu, D. B.; Yin, Q. F.; Xu, D. Y.; Wei, Y. J.; Ding, B. Q.; Shi, X. H. et al. Tunable rigidity of (polymeric core)–(lipid shell) nanoparticles for regulated cellular uptake. *Adv. Mater.* **2015**, *27*, 1402–1407.

[25] Borase, T.; Heise, A. Hybrid nanomaterials by surface grafting of synthetic polypeptides using N-carboxyanhydride (NCA) polymerization. *Adv. Mater.* **2016**, *28*, 5725–5731.

[26] Song, Z. Y.; Han, Z. Y.; Lv, S. X.; Chen, C. Y.; Chen, L.; Yin, L. C.; Cheng, J. J. Synthetic polypeptides: From polymer design to supramolecular assembly and biomedical application. *Chem. Soc. Rev.* **2017**, *46*, 6570–6599.

[27] Shen, Y.; Fu, X. H.; Fu, W. X.; Li, Z. B. Biodegradable stimuli-responsive polypeptide materials prepared by ring opening polymerization. *Chem. Soc. Rev.* **2015**, *44*, 612–622.
[28] Deming, T. J. Synthesis of side-chain modified polypeptides. *Chem. Rev.* **2016**, *116*, 786–808.
[29] Guyon, L.; Lepeltier, E.; Passirani, C. Self-assembly of peptide-based nanostructures: Synthesis and biological activity. *Nano Res.* **2018**, *11*, 2315–2335.
[30] Lindgren, M.; Hällbrink, M.; Prochiantz, A.; Langel, Ü. Cell-penetrating peptides. *Trends Pharmacol. Sci.* **2000**, *21*, 99–103.
[31] Petsko, G. A.; Ringe, D. *Protein Structure and Function*; New Science Press: London, 2004.
[32] Galoppini, E.; Fox, M. A. Effect of the electric field generated by the helix dipole on photoinduced intramolecular electron transfer in dichromophoric α-helical peptides. *J. Am. Chem. Soc.* **1996**, *118*, 2299–2300.
[33] Song, Z. Y.; Fu, H. L.; Wang, R. B.; Pacheco, L. A.; Wang, X.; Lin, Y.; Cheng, J. J. Secondary structures in synthetic polypeptides from N-carboxyanhydrides: Design, modulation, association, and material applications. *Chem. Soc. Rev.* **2018**, *47*, 7401–7425.
[34] Niwa, M.; Kuwagaki, Y.; Yamaguchi, S.; Higashi, N. Effect of the helix macrodipole on surface-initiated N-carboxyanhydride polymerization on gold. *Angew. Chem.* **2003**, *115*, 1883–1885.
[35] Worley, C. G.; Linton, R. W.; Samulski, E. T. Electric-field-enhanced self-assembly of .alpha.-helical polypeptides. *Langmuir* **1995**, *11*, 3805–3810.
[36] Niwa, M.; Morikawa, M. A.; Higashi, N. Controllable orientation of helical poly($_L$-glutamic acid) rods through macrodipole interaction on gold surfaces and vectorial electron transfer. *Angew. Chem., Int. Ed.* **2000**, *39*, 960–963.
[37] Jaworek, T.; Neher, D.; Wegner, G.; Wieringa, R. H.; Schouten, A. J. Electromechanical properties of an ultrathin layer of directionally aligned helical polypeptides. *Science* **1998**, *279*, 57–60.
[38] Chang, Y. C.; Frank, C. W.; Forstmann, G. G.; Johannsmann, D. Quadrupolar and polar anisotropy in end-grafted α-helical poly(γ-benzyl-L-glutamate) on solid substrates. *J. Chem. Phys.* **1999**, *111*, 6136–6143.
[39] Whitesell, J. K.; Chang, H. K. Surface oriented polymers for nonlinear optics. *Mol. Cryst. Liq. Cryst. Sci. Technol. Sect. A* **1994**, *240*, 251–258.
[40] Zhang, C.; Yuan, J. S.; Lu, J. H.; Hou, Y. Q.; Xiong, W.; Lu, H. From neutral to zwitterionic poly(α-amino acid) nonfouling surfaces: Effects of helical conformation and anchoring orientation. *Biomaterials* **2018**, *178*, 728–737.
[41] Chen, C. Y.; Wang, Z. H.; Li, Z. B. Thermoresponsive polypeptides from PEGylated poly-$_L$-glutamates. *Biomacromolecules* **2011**, *12*, 2859–2863.
[42] Frens, G. Controlled nucleation for the regulation of the particle size in monodisperse gold suspensions. *Nat. Phys. Sci.* **1973**, *241*, 20–22.
[43] Sau, T. K.; Murphy, C. J. Seeded high yield synthesis of short Au nanorods in aqueous solution. *Langmuir* **2004**, *20*, 6414–6420.
[44] Murphy, C. J.; Sau, T. K.; Gole, A. M.; Orendorff, C. J.; Gao, J. X.; Gou, L. F.; Hunyadi, S. E.; Li, T. Anisotropic metal nanoparticles: Synthesis, assembly, and optical applications. *J. Phys. Chem. B* **2005**, *109*, 13857–13870.
[45] Groot, R. D.; Warren, P. B. Dissipative particle dynamics: Bridging the gap between atomistic and mesoscopic simulation. *J. Chem. Phys.* **1997**, *107*, 4423–4435.
[46] Yang, K.; Ma, Y. Q. Computer simulation of the translocation of nanoparticles with different shapes across a lipid bilayer. *Nat. Nanotechnol.* **2010**, *5*, 579–583.
[47] Bonduelle, C. Secondary structures of synthetic polypeptide polymers. *Polym. Chem.* **2018**, *9*, 1517–1529.
[48] Li, G. Z.; Cheng, G.; Xue, H.; Chen, S. F.; Zhang, F. B.; Jiang, S. Y. Ultra low fouling zwitterionic polymers with a biomimetic adhesive group. *Biomaterials* **2008**, *29*, 4592–4597.
[49] Banerjee, I.; Pangule, R. C.; Kane, R. S. Antifouling coatings: Recent developments in the design of surfaces that prevent fouling by proteins, bacteria, and marine organisms. *Adv. Mater.* **2011**, *23*, 690–718.
[50] Matsuura, K.; Ohno, K.; Kagaya, S.; Kitano, H. Carboxybetaine polymer-protected gold nanoparticles: High dispersion stability and resistance against non-specific adsorption of proteins. *Macromol. Chem. Phys.* **2007**, *208*, 862–873.
[51] Yu, X. F.; Liu, Z. H.; Janzen, J.; Chafeeva, I.; Horte, S.; Chen, W.; Kainthan, R. K.; Kizhakkedathu, J. N.; Brooks, D. E. Polyvalent choline phosphate as a universal biomembrane adhesive. *Nat. Mater.* **2012**, *11*, 468–476.
[52] Yameen, B.; Choi, W. I.; Vilos, C.; Swami, A.; Shi, J.; Farokhzad, O. C. Insight into nanoparticle cellular uptake and intracellular targeting. *J. Control. Release* **2014**, *190*, 485–499.
[53] Tian, F. L.; Zhang, X. R.; Dong, W. How hydrophobic nanoparticles aggregate in the interior of membranes: A computer simulation. *Phys. Rev. E* **2014**, *90*, 052701.
[54] Yue, T. T.; Zhang, X. R. Molecular understanding of receptor-mediated membrane responses to ligand-coated nanoparticles. *Soft Matter* **2011**, *7*, 9104–9112.
[55] Hou, Y. Q.; Zhou, Y.; Wang, H.; Sun, J. L.; Wang, R. J.; Sheng, K.; Yuan, J. S.; Hu, Y. L.; Chao, Y.; Liu, Z.; Lu, H. Therapeutic protein PEPylation: The helix of nonfouling synthetic polypeptides minimizes antidrug antibody generation. *ACS Cent. Sci.*, in press, DOI: 10.1021/acscentsci.8b00548.